Climate Dynamics (1998) 14:431–450

A. Bacher · J. M. Oberhuber · E. Roeckner

ENSO dynamics and seasonal cycle in the tropical Pacific as simulated by the ECHAM4/OPYC3 coupled general circulation model

Received: 14 June 1996 / Accepted: 11 November 1997

Abstract The new version of the atmospheric general circulation model (AGCM), ECHAM4, at the Max Planck Institute for Meteorology, Hamburg, has been coupled to the OPYC3 isopycnic global ocean general circulation and sea ice model in a multi-century present-day climate simulation. Non-seasonal constant flux adjustment for heat and freshwater was employed to ensure a long-term annual mean state close to present-day climatology. This study examines the simulated upper ocean seasonal cycle and interannual variability in the tropical Pacific for the first 100 years. The coupled model's seasonal cycle of tropical Pacific SSTs is satisfactory with respect to both the warm pool variation and the Central and Eastern Pacific, with significant errors only in the cold tongue around April. The cold phase cold tongue extent and strength is as observed, and for this the heat flux adjustment does not play a decisive role. A well-established South Pacific convergence zone is characteristic for the new AGCM version. Apart from extending the southeast trades seasonal maximum to midbasin, wind stress pattern and strength are captured. Overall the subsurface structure is consistent with the observed, with a pronounced thermocline at about 150 m depth in the west and rising to the surface from 160 °W to 100 °W. The current system is better resolved than in some previous global models and, on the whole, has the expected shape. The equatorial undercurrent is correctly positioned but the core is only half as strong as observed. The north equatorial current and countercurrent also have reduced maximum speeds but the April minimum is captured. As with the companion publication from Roeckner et al. this study finds pronounced tropical Eastern and Central Pacific interannual variability. Simulated and observed NINO3 sea surface temperature (SST) variability is represented by a single, rather broadband, maximum of power spectral density, centered on about 28 months for the simulation and four years for the observations. For simulation and observations, SST, windstress, and upper ocean heat content each exhibit a single dominant large-scale amplitude and phase pattern, suggesting that the model captures the essential dynamics. The amplitude of the essentially standing oscillation in SST in the NINO3 region attains the observed strength, but is weaker at the eastern boundary. Anomalies of upper ocean heat content show off-equatorial westward and equatorial eastward propagation, the latter's arrival in the east of the basin coinciding with the SST anomalies. Equatorial wind stress anomalies near the date line provide the appropriate forcing and clearly form a response to the anomalous SST.

A. Bacher (✉) · E. Roeckner
Max-Planck-Institut für Meteorologie, Bundesstraße 55,
D-20146 Hamburg, Germany
E-mail: bacher@dkrz.de

J. M. Oberhuber
Deutsches Klimarechenzentrum GmbH, Bundesstraße 55,
D-20146 Hamburg, Germany

1 Introduction

The El Nino/Southern Oscillation (ENSO) is the dominant natural climate variation in the tropics over time scales of a few years. Expressing itself in the recurrent weakening and eastward/equatorward migration of tropical Pacific convergence zones in conjunction with anomalously warm Eastern and Central Pacific SSTs, it also influences extratropical features of the general circulation and ultimately induces a near-global climate signal. In climate models used for the simulation of climate change, the validity of model results pertaining to ENSO is a major concern and should be assessed within present-day climate simulations.

Simulations primarily aimed at studying tropical ocean-atmosphere variability have been done with coupled ocean-atmosphere models of varying complexity. Models with restricted domain and a simplified atmospheric component but shallow water ocean dynamics or an ocean general circulation model (OGCM) have simulated variability identifiable with ENSO, and were used to formulate the oscillator concept of Suarez and Schopf (1988) and Battisti and Hirst (1989), or the propagating SST modes described by Neelin (1991); see Neelin et al. (1994) for an overview of theoretical concepts and references. *Global* coupled GCMs (CGCMs), of similar type as used in this study, had not succeeded in realistically simulating ENSO at the time when Neelin et al. (1992) reviewed coupled modelling of ocean-atmosphere interactions in the tropics.

Meanwhile, a number of studies have been published showing results of extended CGCM integrations, with global or near-global extent in both the atmosphere and the ocean component, qualitatively resembling ENSO dynamics more closely although generally with weaker amplitudes than observed (e.g. Meehl 1990; Lau et al. 1992; Nagai et al. 1992; Latif et al. 1994; Lunkeit et al. 1996; Tett 1995; Knutson and Manabe 1994).

The majority of CGCMs with the entire globe as the active domain in multi-decadal simulations have included flux adjustments (or, 'corrections') (Sausen et al. 1988) in the formulation of the coupling interface. The major motivation includes regional modelling problems, such as an unrealistic seasonal cycle of sea ice or inadequate simulation of the thermohaline circulation in characteristic high-latitude regions, as well as large-scale drift toward a new equilibrium state after coupling the two components, generally following an ocean-only integration toward uncoupled equilibrium. These constant corrections of monthly mean fluxes, generally of heat and freshwater fluxes, and often wind stress, sometimes also of SST and ice mass (e.g., Manabe et al. 1991, Cubasch et al. 1992, Lunkeit et al. 1996, Murphy 1995) are designed to constrain the climatology of the model, while ocean and atmosphere interact through anomalies, an approach which generally substantially reduces drift.

When using seasonal flux adjustment, the ability of the model to simulate a realistic seasonal cycle in the tropics is of no fundamental interest. However, the seasonal cycle can have links to ENSO in various ways. Apparently some phase-locking occurs, with the initiation of warm events mostly in Northern Hemisphere spring. In an uncoupled OGCM forced by observed winds, Barnett et al. (1992) found that low frequency variability seemed not to be directly driven by a seasonal cycle however the system was more sensitive to perturbations at some times of the year than at others. In a recent theoretical investigation, Jin et al. (1994), using a stripped-down intermediate model, suggest that the quotient of ENSO and annual periods assumes discrete values given by ratios of small integers, as model parameters are continuously varied, which ultimately leads to chaos. For coupled modelling of tropical atmosphere-ocean dynamics it is certainly desirable to achieve a freely simulated seasonal cycle. A recent comparison of several CGCMs (Mechoso et al. 1995), each integrated over about a decade, was restricted to cases where no flux adjustment was used (longer integrations are described e.g., in Latif and Barnett 1994 or Robertson et al. 1995a,b). Despite some substantial shortcomings such as a doubling of the ITCZ in some models or its seasonal intrusion well into the Southern Hemisphere in others, as well as a common tendency toward extending the cold tongue significantly into the warm pool, these results certainly represent progress in coupled modelling in the tropics by GCMs, as compared to the earlier review (Neelin et al. 1992).

Here we present results on tropical ocean-atmosphere dynamics obtained with a global atmosphere-sea ice-ocean GCM in the course of a multi-century present-day climate simulation. We have applied globally only annual mean flux adjustment restricted to heat and freshwater, thus leaving the determination of the seasonal cycle up to the model physics. Since in a companion paper (Roeckner et al. 1996b), aspects of the simulated atmospheric seasonal evolution and space-time variability connected to ENSO both in the tropics and extratropics are discussed separately, we here focus attention on model results on the upper tropical Pacific ocean seasonal cycle and interannual variability. The demonstration of the stability of simulated control climate including sea ice, and further aspects of climate variability, will be the subject of forthcoming publications.

The remaining four sections proceed as follows. First we give a summary of the coupled model and essentials of the coupling strategy. The next two sections are concerned, respectively, with discussing the simulated upper tropical Pacific seasonal cycle in temperature, currents, and forcing by the AGCM, and with highlighting the spatio-temporal characteristics of the simulated ENSO dynamics. Both sections provide comparison with observations. Finally we state conclusions from our present study.

2 Global coupled model and flux adjustment

The AGCM and OGCM component, as well as the technique of coupling, represent most recent developments; the coupling of earlier versions of the component models by a different technique, involving seasonal flux adjustment essentially for all quantities exchanged between them, is described by Lunkeit et al. (1996).

The AGCM component is the ECHAM4 general circulation model developed at the Max Planck Institute for Meteorology. It is the current generation in the line of ECHAM models (Roeckner et al. 1992) which evolved from the European Centre for Medium Range Weather Forecast (ECMWF) model under extensive reconstruction in parametrizations for processes such as soil processes, local runoff, simple prognostic sea-ice skin temperature, boundary layer physics, prognostic cloud liquid water and ice. A summary of

recent developments regarding model physics in ECHAM4 and a description of the simulated climate obtained with the uncoupled ECHAM4 model is given in Roeckner et al. (1996a). These new features include use of the more recent radiation scheme from the ECMWF model (Morcrette 1991), modified to include additional greenhouse gases, and with revised water vapor continuum absorption (Giorgetta and Wild 1995); introduction of a higher-order turbulence closure (Brinkop and Roeckner 1995); modified mass flux convection and cloud entrainment/detrainment (Nordeng 1996 submitted); and a supplement in the stratiform cloud scheme.

The prognostic variables, vorticity, divergence, temperature and surface pressure are represented as expansions in spherical harmonics with triangular truncation at wavenumber 42 (T42). Starting with ECHAM4, advection of prognostic water vapor and cloud liquid water/ice are treated by a semi-Lagrangian scheme. The physical parametrizations run on a 128×64 (longitude $\times$ latitude) Gaussian grid yielding a meshwidth of approximately 2.8°. In the vertical, 19 hybrid σ-p levels are used extending from the topography to 10 hPa. The time step is 24 minutes except for radiation which uses 2 h.

The OGCM component is an updated version of the OPYC general circulation model by Oberhuber (1993). It solves the primitive equations in the form of conservation laws for momentum, mass, heat and salt on isopycnal layers, with a realistic equation of state, and the sea level, given by vertical summation of layer thickness at any time, evolving freely. Diapycnal and isopycnal mixing are parametrized, respectively, using a Richardson-number dependent criterion and Laplacian diffusion with temporally and spatially varying coefficients. The latter for momentum depend on local Rossby-radius, for scalars on the local deformation of the flow field. The convective adjustment completely removes unstable stratification in one time step.

A mixed layer using the same governing equations as the interior ocean, but with a detailed calculation of turbulent entrainment/detrainment based on turbulent kinetic energy input by wind stirring, buoyancy flux due to heat and freshwater, and local shear is included as the top layer with an arbitrary potential density and a minimum thickness of 10 m. A fraction of solar radiation is allowed to penetrate below the mixed layer.

Sea ice and snow cover is predicted in the form of grid-cell averaged thicknesses and a common area concentration, together with an equation of motion neglecting momentum advection and using viscous-plastic rheology in the stress term (Hibler 1979). A simple computation of ice and snow top temperatures and thermodynamic mass tendencies provides input to the prognostic equations.

In uncoupled simulations, surface fluxes everywhere are entirely given by bulk laws involving observed climatological atmospheric quantities and simulated surface temperature (Oberhuber 1988, 1993), but surface salinity forcing includes Haney (1971) type restoring in addition to precipitation and evaporation with a restoring time constant of about 12 days.

The diurnal cycle is omitted, and half a day is used in the semi-implicit time stepping. The scalar gridpoints of an Arakawa B-grid coincide with those of the AGCM grid except equatorward of 36° latitude where the meridional spacing is gradually decreased to approximately 0.5° (1.0°) equatorward of 5° (10°) latitude to resolve the equatorial waveguide. Including the mixed layer, 11 layers are used.

The models are coupled quasi-synchronously, exchanging daily averaged quantities once a day. The AGCM receives the mixed layer temperature and the scalar sea-ice variables without any adjustment. For the OGCM, downward solar radiation, river discharge, wind stress, and the cube of the friction velocity, $u*^3$, are passed, again without adjustments. $u*^3$ is passed separately since deriving it from daily mean wind stress would lead to underestimation of the turbulent kinetic energy input to the mixed layer. River discharge is computed by the river routing scheme of Sausen et al. (1994) using grid cell runoff as computed in ECHAM. The other parametrizations are detailed in Roeckner et al. (1996a). The flux adjustment in heat and freshwater will reflect the difference of flux delivered by the AGCM and flux requested by the OGCM in the long-term annual mean.

To achieve global consistency in the annual mean flux adjustments, including heat flux in the presence of ice, we mainly adopted a scheme that OPYC provides for obtaining heat and freshwater flux adjustments in runs with a coupled energy balance model. Essentially, in this scheme, the OGCM, as well as the AGCM, both have to supply simultaneous independent estimates of these fluxes during the process of determining the adjustment (see later) in a coupled integration preceding the main simulation. For freshwater, OPYC uses climatological precipitation and latent heat flux from its bulk parametrization, whereas precipitation minus evaporation is delivered by ECHAM. The heat flux treatment was somewhat revised for the present integration, in that the bulk formulae in OPYC are combined with an alternative formulation for the heat transfer through sea ice and snow cover. Where these exist, a continuous profile of thermal diffusive flux is matched to the surface heat flux and SST prescribed at the freezing point, and with these assumptions, a prediction for the skin temperature and an ice mass tendency term are derived; an additional budget term for melting snow or bare ice is stored when the skin temperature reaches 0 °C. This scheme is implemented in ECHAM also and determines the boundary temperature for the lowest atmosphere layer on sea-ice points, and ensures that OPYC is passed either the net heat flux in ice-free areas, or the thermodynamic ice and snow mass tendencies elsewhere. The heat flux adjustment then applies universally to the mixed layer heat balance and, thus, in cells with ice relates to the ice mass tendency. Snow mass is not subject to heat or freshwater flux adjustments.

In order to spin up the OGCM, approximately 1000 y of ocean-only integration were conducted with the uncoupled setup described, but including ice modifications and others, as detailed next. Over the first 500 y observed climatological quantities, such as air temperature, were inserted into the bulk laws in OPYC, although the full daily wind stress was taken from an uncoupled integration of the ECHAM3 AGCM with observed SST from 1979–1988 (ECHAM4 was still under construction). Subsequently, day-to-day variability in the form of anomalies of net heat flux and precipitation minus evaporation anomalies from ECHAM3 was added, since full values would lead to problems at the ice edge which varies during spinup but was fixed during the ECHAM3 run.

Next follows a transition phase of coupling with continuously updated flux adjustments. We denote F_A the flux, heat or freshwater, passed by the AGCM, F_O the flux resulting from the OGCM bulk parametrization under the same surface conditions. F_{rest} is the Haney (1971) type restoring term which for the present setup was introduced also for heat, except where ice exists, in the form $\alpha\ (SST_{obs} - SST_{mod})$, with α dependent on SST as in Oberhuber (1988) yielding a restoring time scale of the order of two months. Then the flux F seen by the OGCM in the final phase (fixed flux adjustment) is

$$F = F_A + \langle F_O + F_{rest} - F_A \rangle,$$

where the second term on the right represents a long-term annual mean. The transition phase is used to estimate initially this term on a daily update basis and then to relax smoothly to only annually updated estimates in the form of averages over all completed years. For both flux adjustment fields, extending the transition phase over 100 y yielded sufficiently well-defined expectation values of the sequences of yearly updates, despite tendencies for local cyclostationarity in the freshwater flux adjustment estimates. The fully coupled run with adjustments fixed was then initialized with the state at the beginning of year 91. Basics of the scheme for spinup and transition phase are displayed in Fig. 1.

Since in the tropics the two model grids differ as stated, particular care has been taken to convert the fluxes passed by the AGCM in a conserving way. A numerically efficient scheme has been developed which respects positivity, e.g., for $u*^3$ or river discharge, and

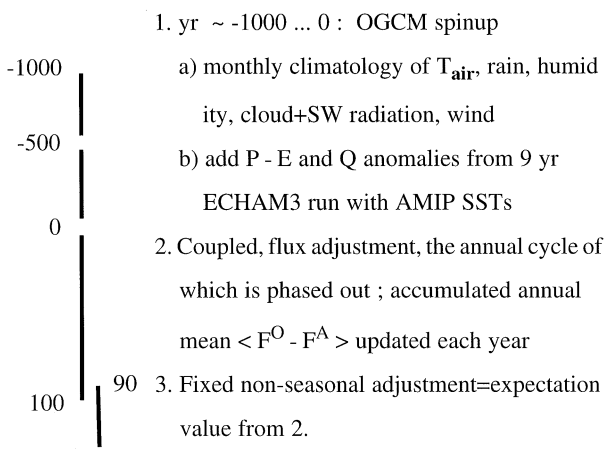

Fig. 1 Basic coupling scheme due to Oberhuber

guarantees exact local conservation. A more detailed description is deferred to a future publication.

3 Seasonal cycle

Since only annual mean flux adjustment is used, a reasonable effort can be made to validate the seasonal cycle of tropical Pacific temperature and currents and the momentum and heat fluxes. The outcome will also determine whether some confidence can be placed on disturbances of currents and thermal structure on interannual time scales.

Tropical Pacific SSTs and turbulent heat fluxes are coupled locally with negative feedback; radiative fluxes influence SSTs due to the seasonal migration of the sun and complex feedbacks involving clouds. The strong equatorial surface currents modify SSTs considerably, in particular due to cold upwelling in the east caused by divergence of surface flow. In what follows the emphasis is on large scale structures as well as some attribution of results of the SST analysis to the connection with other variables.

3.1 SST

Figure 2 shows the observed and simulated sea surface temperature (SST) for all three oceans. For the simulation, the first 100 y (91–190) were used. The observations are taken from the global ice and sea surface temperature (GISST) dataset, version 2.2 (Rayner et al. 1995), for which each month was averaged over the period 1951 through 1975. Following Horel (1982) we show only the seasonal deviation i.e., we use the difference between full field and annual mean, and from this difference we subtract its zonal average, multiplied by $|\sin\varphi|/(\sin 30°)$. Additionally, lighter (darker) shading indicates areas where total SSTs are greater than 27 °C (29 °C).

In the tropical Pacific, the observed annual cycle is strongest in the east, where the equatorial cold tongue has minimum strength in the month of April and is strongest in September. For the Western Pacific warm pool, annual/semiannual cycles imply that the proportion north of the equator, of the region of maximum SSTs (> 28 °C), is only minor for January to March but major for July to September. Our choice of four months includes April and October as found in a recent study comparing coupled GCM results in the tropical Pacific (Mechoso et al. 1995). The inclusion of January and July permits limited reference to the phasing of the seasonal cycle.

In all four months in the simulation the southeastern extension of the region warmer than 27 °C is limited at about 120 °W. For the West Pacific, the northeastward extent of the NH portion of waters with temperatures above 27 °C is captured in July but its southward retreat is simulated about a month too early. Also, the simulated westward extent of the cold tongue in each month compares favorably to the observed, and in the vicinity of the dateline never cools below 28 °C. Important for the atmospheric circulation (which via low-level winds feeds back on equatorial upwelling and hence SST) is the finding that the zonal SST gradient in July and October in the Central and Western Pacific is somewhat stronger than observed. From January to April the model captures the general warming of the Eastern Pacific and the associated retreat of the cold tongue. The simulation exhibits a cold bias near 110°W in April when the seasonal maximum is attained but the temperature is simulated 2 K too cold. While we defer additional comments to Sect. 3.4, we note that not many of the current coupled GCMs correctly reproduce the boreal spring temperatures in the cold tongue (Mechoso et al. 1995, Robertson et al. 1995). Some also underestimate them in boreal fall, thus yielding a colder mean state but alleviating errors in the seasonal deviation. The seasonal deviation on the equator is commonly rendered for the equator as a time-longitude Hovmoeller diagram. For the observations, for January to May the maximum rate of warming is found in the Eastern Pacific and this induces a westward spreading of a zone of seasonally anomalous west-east SST gradient. This qualitatively results for the present model, too, but with a dip at 110°W (not shown).

3.2 Heat flux

Some of the features in the simulated SST can be related to the atmospheric forcing by wind stress and net heat flux, i.e., the sum of long- and shortwave net radiation and latent and sensible turbulent fluxes. In the determination of the seasonal cycle of most of the upper tropical Pacific the forcing by wind stress and heat flux (including latent heat flux) dominates over the

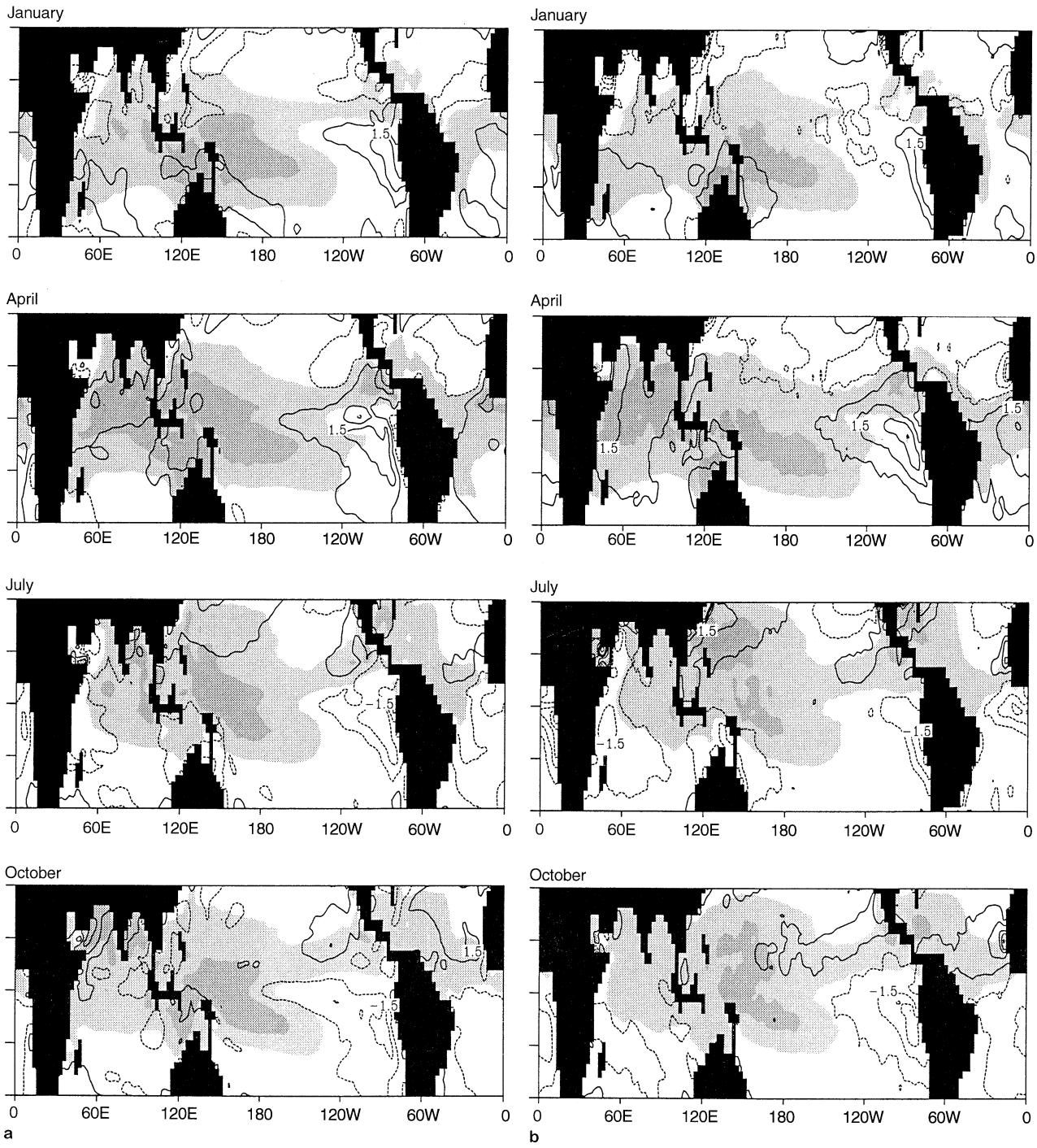

Fig. 2a, b Monthly mean SST (January, April, July, October) for **a** coupled model, y 91–190; **b** GISST 2.2 data, 1951–1975. The seasonal deviation is shown computed as in Horel (1982), i.e., after subtracting annual mean and zonal average times $|\sin \varphi|/(\sin 30^\circ)$. Additionally, *lighter* (*darker*) *shading* indicates areas with total SST greater than 27 °C (29 °C). Latitudes 15 °N, 15 °S, and 30 °N, 30 °S are marked along the *left hand border*

freshwater flux (Schneider and Barnett 1995); precipitation has been shown as annual mean by Roeckner et al. (1996b). Figure 3a–d) shows a comparison with Oberhuber's (1988) estimates of net heat flux for the extreme months of January and July and the annual mean.

Annual means (Fig. 3. a, b) will be compared first and put into perspective with the flux adjustment (Fig. 3c) but subsequently the relation to the seasonal cycle will also be considered. The general agreement is quite satisfactory, bearing in mind the sparsity of measurements

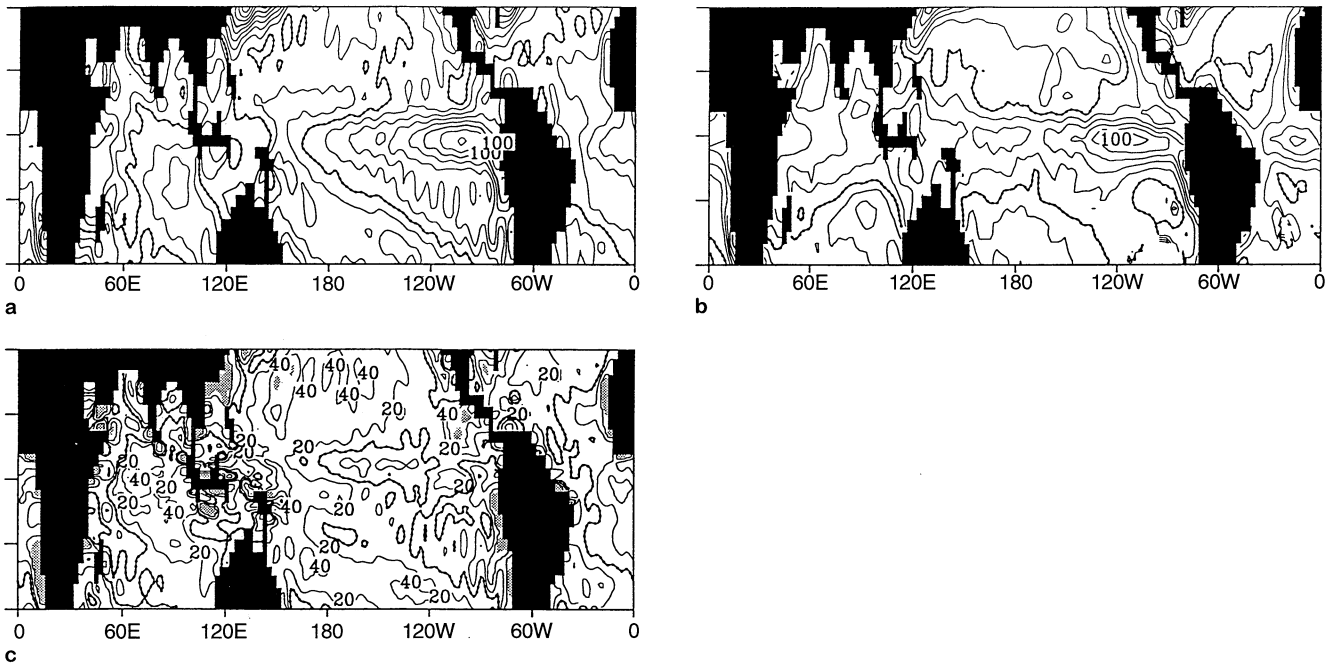

Fig. 3a–c Mean net heat flux **a** as passed from AGCM un-flux-adjusted, annual mean; **b** Oberhuber climatology annual mean; **c** heat flux adjustment. Contour interval 20 Wm^{-2}. In **c**, *shading* indicates values beyond $\pm$ 60 Wm^{-2}. Latitudes as in Fig. 1

in the southeastern subtropical Pacific, particularly in July. Wave-like structure in the simulation results originates from the truncated spectral representation of the orography including the sea surface in the AGCM. In the area between Papua New Guinea and the date line, a difference of around 30–40 Wm^{-2} is seen. In the West Pacific warm pool region, we can, thus, to some extent, relate the required flux adjustment heat input to the forcing by the AGCM. From first inspection of individual heat flux components and analysis of an uncoupled integration of the AGCM (Chen and Roeckner 1996a, b), stronger than observed latent heat flux or high cloud albedo is likely to be the primary contribution. However, these publications have used different observed heat flux datasets which indicate heat flux closer to zero in the equatorial Western Pacific than estimated by Oberhuber (1988). The rather homogeneous distribution of heat flux adjustment in the North Pacific with heat input of 30–40 Wm^{-2} required does not have a counterpart in the present comparison of simulation and observational estimates. Since the bulk parametrizations in the OGCM are very similar to those used in the present observed estimates, we attribute this to the contribution of averaged F_{rest} to the flux adjustment. In the core of the cold tongue, the AGCM heat flux exceeds observational estimates by about 40 Wm^{-2}, consistent with a shifted heat balance by reduced latent heat flux. This is suggested by the cold bias in SST, primarily in Northern Hemisphere spring, and by wind strength not exceeding the observed in the far Eastern Pacific, as discussed later.

Overall, the non-seasonal heat flux adjustment, having typical magnitudes at the lower end compared to other (seasonally) flux-corrected CGCMs (e.g., Tett 1995) does not show strong spatial structure, e.g., over the annual mean cold tongue (north of which there is only a shallow minimum). In the southeastern Pacific, however, it contributes a cooling term which peaks near the coast. This can be related to shortcomings of the simulation of the seasonal cycle. This is the failure of the OGCM to resolve coastal upwelling as well as a, probably somewhat underestimated, stratus cloud cover for the second half of the year, with the former significantly enhancing the latter because coastally upwelled water would experience Ekman drift and cool a broader off-coastal region. Since this advectively influences the equatorial Eastern Pacific, sufficient coastal upwelling and a stronger stratus response would help prevent the cold phase of the equatorial cold tongue being terminated by insolation in October. An additional positive feedback may tie in with the advective cooling, through zonal SST gradient enhancing the strength of the southeastern trades on the equator and thus cold equatorial upwelling. Thus the shortcomings noted might provide a partial explanation for the slight warm bias in the east in January, assuming this is an expression of a premature warming phase. Also there are similar problems with these sensitive feedbacks in most other CGCMs (Mechoso et al. 1995).

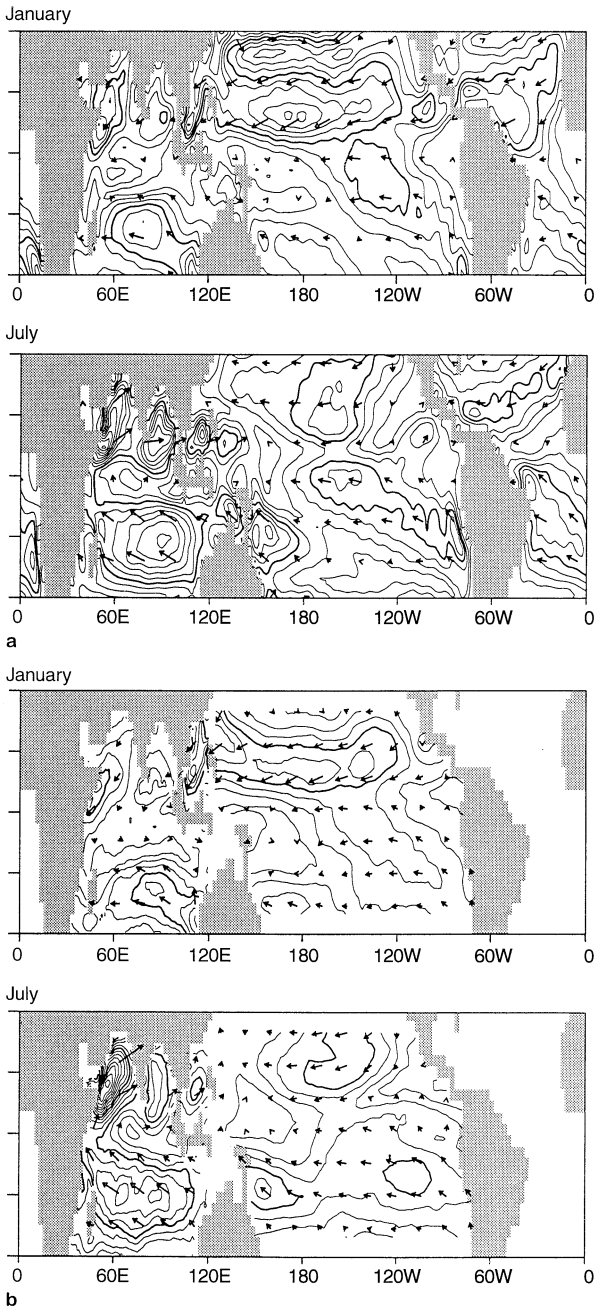

Fig. 4a, b Mean wind stress **a** coupled model, for January and July; **b** FSU data for January and July, multiplied by 1.5×10^{-3} kg m^{-3}. Contours for magnitude at intervals of 0.02 Nm^{-2}; *thick contours* for 0.08 Nm^{-2} (and multiples thereof). Latitude marks as in Fig. 1.

3.3 Wind stress

Figure 4 shows January and July mean wind stress for the simulation and pseudo-stress for 1970 through 1994 in the Indian ocean and 1961 through 1994 in the Pacific, from the FSU atlas (Stricherz et al. 1992, 1993). Using these months is consistent with our discussion of SST, although the observed wind stress in the south-eastern Pacific increases by about a further 10% from July to August, with a concomitant decrease in the NH at about 15 °N. In the simulation there is less difference between July and August. Since the FSU stress is given without air density and drag coefficient, we performed a comparison for the CGCM data by computing approximate average values of squared 10 m wind speed over simulation years 121 through 150, using the twice-daily output of instantaneous wind velocity for the lowest layer and the roughness length. On dividing the proper wind stress, accumulated from all time steps, by this square wind speed estimate, the resulting product of air density and drag coefficient over most open ocean areas shown here deviates from about 1.5×10^{-3} kg m^{-3} by at most 15%. To ease comparison, this was applied as a constant factor to the FSU pseudostress. For January, simulation and observations show good agreement, with a tendency for slightly stronger winds in the model.

For July, stronger observed winds are found over the Arabian Sea, while in the Pacific the SH maximum in the simulation is extended northwestward in relation to the observed distribution. The latter seems to relate to the positive feedback mentioned in the preceding section, namely that upwelling-induced east-west SST gradient enhances wind stress west of the cold upwelling region which consequently spreads westward. Nevertheless, the overall wind pattern and strength is simulated realistically, in particular, the simulation produces a realistic slanting of the SPCZ. A problem in several coupled GCMs has been that the region of convergence tended to evolve into a narrow zonal cross-basin shape south of the equator mirroring the ITCZ, particularly in integrations without flux adjustment (Mechoso et al. 1995). In the present AGCM version a modified closure in the cumulus convection scheme linking penetrative convection to convective available potential energy (CAPE) rather than moisture convergence is used (Nordeng 1996) which results in a closer link of convection to forcing by SST.

3.4 Vertical structure

For the following discussion of vertical temperature and current distributions it is important to treat the layer-based variables in accordance with the conservation laws expressed in the OGCM equations. At each time step we employ a transformation algorithm from isopycnal to space-time-invariant Z-layers which at each (x, y) location preserves vertically integrated $\rho \times \Psi$ where Ψ is T, u, v. The algorithm avoids large zero-order discontinuities as would result if Z-layers were simply assigned values from corresponding isopycnal layers with linear weighting near isopycnal interfaces, but continuity of the vertical derivative is sacrificed to substantially reduce (but not altogether eliminate, see Fig. 5a–c) spurious oscillations in the vertical.The eleven layers are mapped into 33 Z-layers

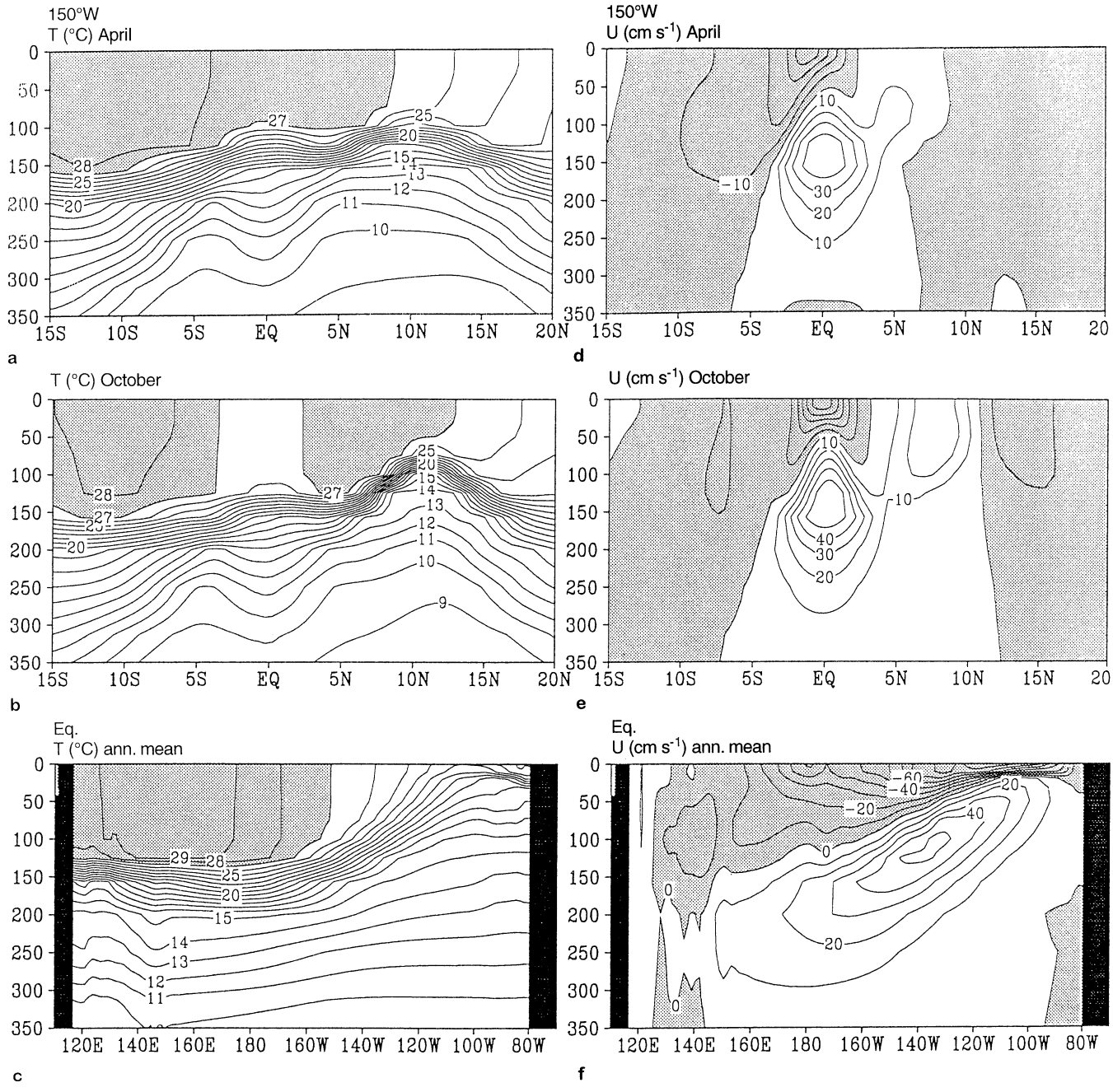

Fig. 5a–f Meridional temperature section at 150° W for April; **b** as **a** but for October; **c** annual mean temperature section along the equator; **d**, **e**, **f**, as **a**, **b**, **c** but for zonal velocity. Contours at intervals of 1 K for temperature and at 10 cm s^{-1} for velocity; *stippling* indicates regions warmer than 27 °C, or where motion is westward

with midpoints corresponding to the Levitus (1982) dataset. The upper 350 m in the tropics are typically covered by the mixed layer and five isopycnal layers which transform into 12 Z-layers.

After time-averaging the transformed $\rho \times \Psi$ and ρ, the quotient yields mass-weighted temperature and currents and vertically integrated mass flux divergence divided by density, representing vertical velocity but including any turbulent processes. Sections of these quantities along the equator and along 150 °W are shown in Figs. 5 and 6.

An observational feature the simulation reproduces successfully is a pronounced thermocline at about 150 m depth in the west with upward sloping isotherms east of about 160°W. When compared to the Hawai to Tahiti shuttle data (Wyrtki and Kilonsky 1984) the

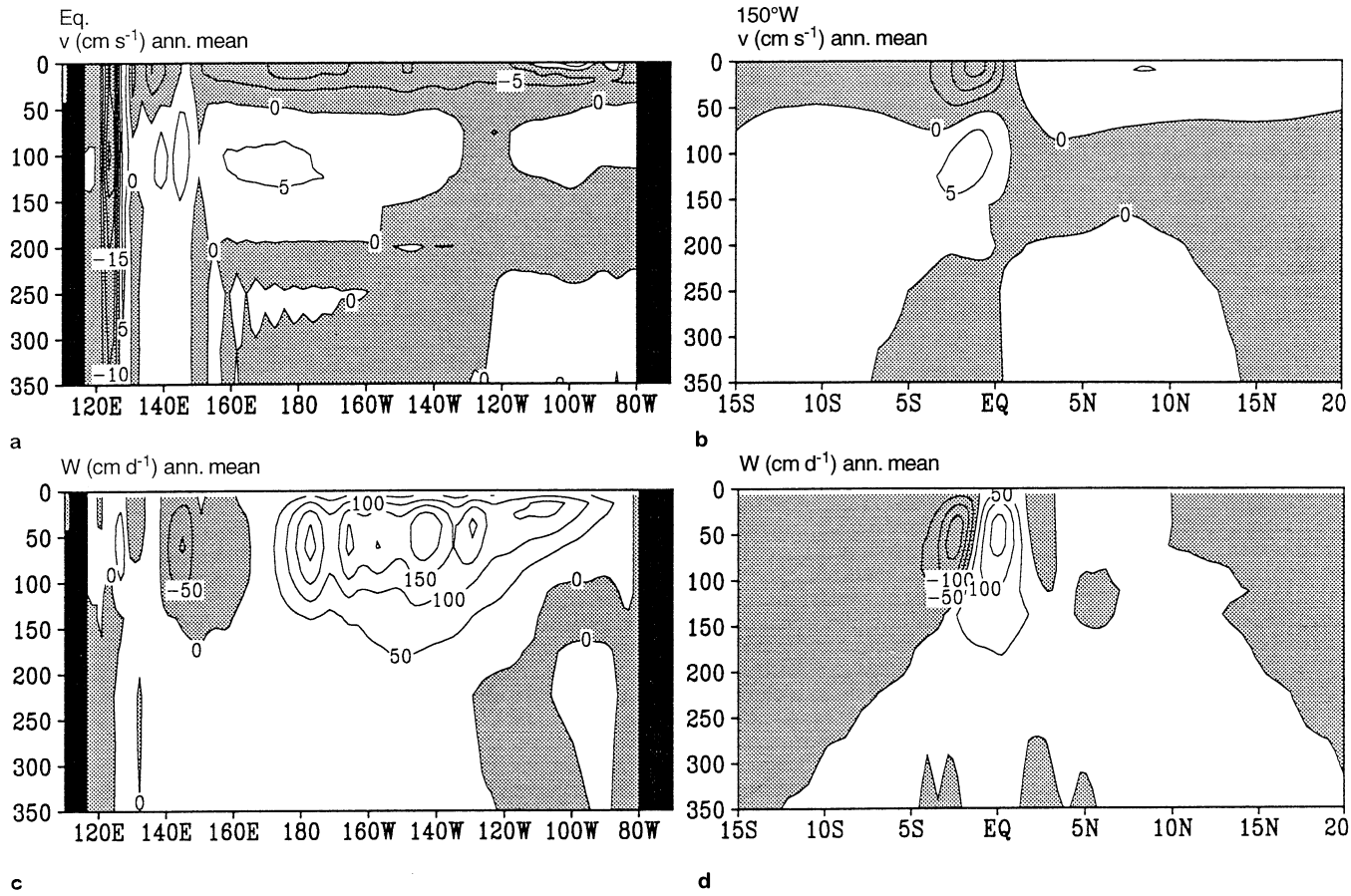

Fig. 6 **a** Section of annual mean meridional velocity along the equator; **b** meridional section of annual mean meridional velocity at 150 °W; **c**, **d** as **a**, **b**, but for vertical velocity. Contours at intervals of 5 cm s^{-1} for meridional velocity and at 50 cm d^{-1} for vertical velocity; *shading* indicates regions of southward or downward motion

meridional section (Fig. 5a, b) shows that even the relatively few upper ocean layers because of the freedom to adjust their local thickness manage to capture the observed structure above 300 m. As expected from SST, the asymmetry close to the equator near the surface is more marked in April than in October. Consistent with the discussion of the seasonal cycle of model SST, in the zonal section of temperature (Fig. 5c), near 110 °W too many isotherms reach the surface. This is due to a tendency in the model to simulate a too shallow thermocline, particularly around northern spring. The reasons for this are still under investigation. The highly sensitive region of shoaling isotherms in the east certainly is a problem in global OGCMs to date.

Using geostrophic arguments modified near the equator as suggested by Picaut and Tournier (1991), the meridional section of the zonal current (Fig. 5d, e) appears consistent. In particular, as described variously (e.g., Reverdin et al. 1994 and references therein), the North Equatorial Current (NEC) and the North Equatorial Countercurrent (NECC) are both weak in April. The Equatorial Undercurrent (EUC) appears to have the core in correct position but underestimated by about a factor of 2; the same reduction as apparent with the seasonal values of the NECC and NEC. The latter may also show effects of the variable meridional grid spacing which increases from about 0.7 ° at 5 °N to 1.5 ° near 15 °N. Latitudinally the simulated EUC is wider than observed. This indicates that momentum diffusion probably acts too strongly in the model.

The meridional velocity at 150 °W (Fig. 6a, b) is given as annual means corresponding to the display of observations for this quantity in Reverdin et al. (1994). The strength is acceptable, but the asymmetry in the mean state is not well supported by the observations. Near zero values are obtained across the NECC, whose orientation in nature correlates quite well with the zone of minimum wind speed associated with the ITCZ. Although this is far from being a complete explanation, the simulated wind stress minimum near 150 °W is indeed virtually zonal in July (Fig. 4) and October (not shown), which relates to the aforementioned pattern of southeastern trades in boreal summer. Vertical motion has a well-defined meridional maximum on the

equator; it is dominated by the meridional divergence term and is confined to a region close to the surface (Fig. 6a, b). Off-equatorial downwelling regions correspond to the upwelling on the equator. Overall, as with temperature, the tropical upper Pacific current structure as simulated should permit adequate representation of the evolution of ENSO-type disturbances in our global CGCM.

4 ENSO-related dynamics

4.1 NINO3 variability

We can gain a first impression of ENSO-like behavior from the time series of anomalous SST, averaged over the NINO3 region. The simulated time series and that obtained from the GISST 2.2 dataset are shown as unfiltered monthly means in Fig. 7a, b. We note several similar aspects of the two time series. First, the model seems to produce a signal of similar strength to that seen in the observations. Both series show variance fluctuations over long time scales. Thus, from the seventh decade of the simulation (year 151 onwards) the amplitude is overall stronger than in the earlier part, while the signal strength in the observed record is less before about 1950 with an apparent strengthening in the last three decades. (Of course, if anything, a smaller amplitude, or more noise, in the earlier period than in the latter should be expected from deficient resolution and temporal non-uniformity of the measurements.) Also, both series show extended periods where the signal seems absent, e.g., over a decade in the simulation starting from year 103, or from 1933 through 1940 and 1943 through 1949 in the observations.

Both simulated and observed variability is dominated by interannual time scales. It now appears natural to examine the spatio-temporal variability in two complementary approaches, with the observations and the simulation subjected to identical methods of analysis. First, we focus on the problem of assigning a time scale to the NINO3 timeseries on the basis of their power spectra. In Sects 4.2 and 4.3 we analyze aspects of the coupling of winds and upper ocean thermal structure with some emphasis on equatorial wave dynamics. This is illustrated both by time-longitude sections and by a statistically optimal amplitude-phase pattern analysis which cannot represent the actual dynamical state of the upper ocean at any particular time but for signal propagation gives the direction. Moreover it brings out the coherence in the set of quantities which will comprise SST, zonal wind stress and upper ocean heat content.

Figure 8 shows the power spectral densities (PSDs), of the NINO3 time series from Fig. 7. Concerning trend removal, in the simulation the trend is insignificant; a straight-line fit is subtracted. For the observations, linear de-trending insufficiently removes very low frequency power, with adverse effects, such as power leakage and possible shifting of the peak frequency, on the spectrum estimate. Instead we subtract the output of a low-pass filtering by an algorithm identical to that in Sect. 4.3, where half-power at one year will be used. For de-trending we use half-power at 1/(50 y) which can be achieved by a smoothing cubic spline (Reinsch 1967) with a correction eliminating strong distortions of the fit towards the ends of the input data, resulting from the

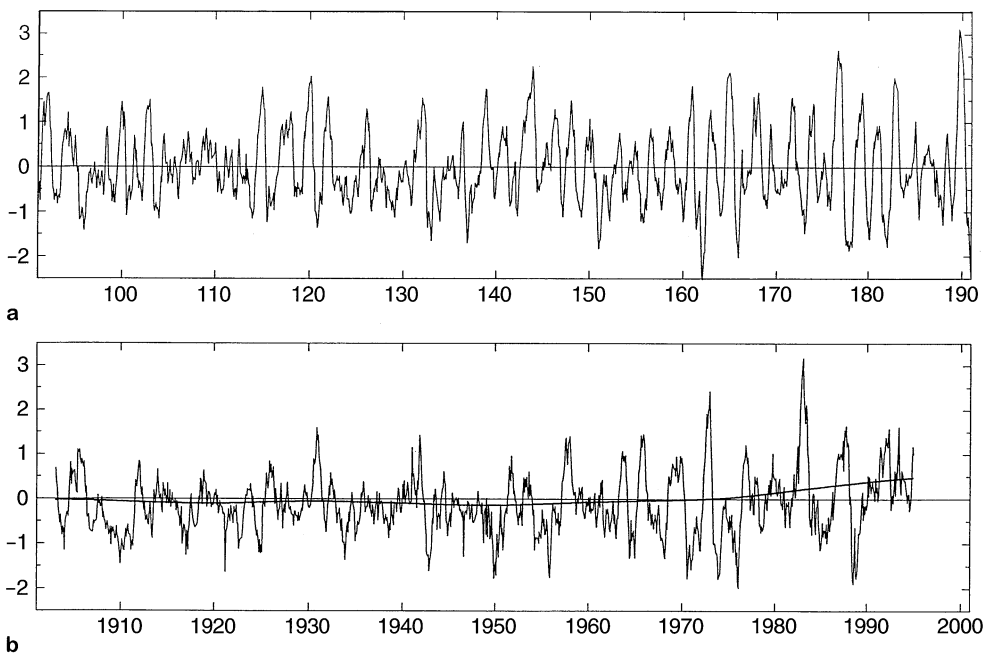

Fig. 7a, b Average SST anomaly NINO3 region, **a** coupled model, **b** GISST 2.2 dataset. In **b**, the *thick curve* shows trend and marginally resolved multi-decadal variablility as output by filtering with frequency response shown as the *left curve* in Fig. 8. *Ticks* mark the beginning of a year

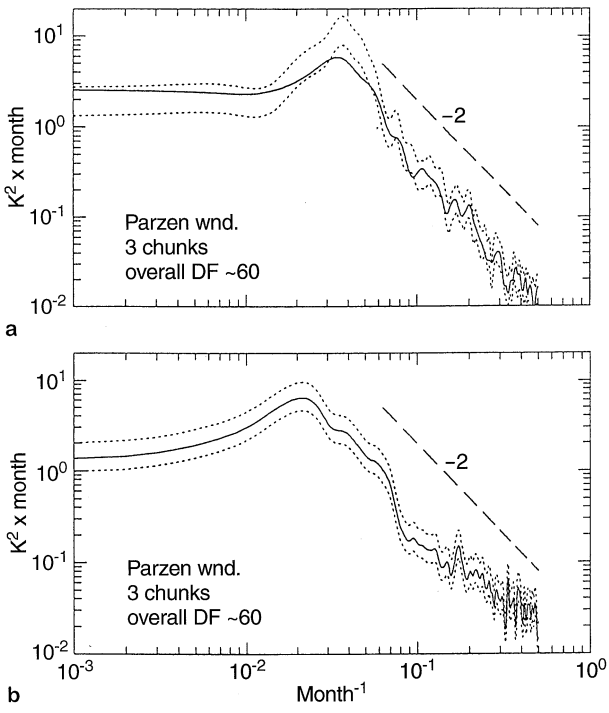

Fig. 8a, b Power spectral density of unsmoothed average SST anomaly NINO3 region, **a** coupled model, **b** GISST 2.2 dataset, after eliminating unresolved low frequency variability and trend

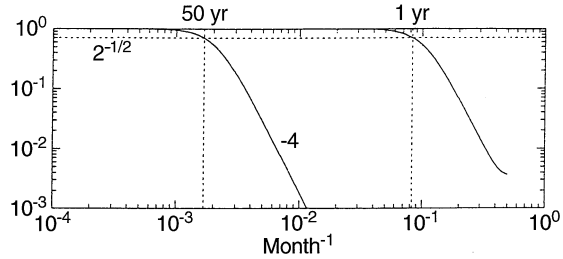

Fig. 9 Filter frequency response used to obtain the *thick curve* in Fig. 6b (*left response curve*), and for light smoothing of data prior to the analyses illustrated in Fig. 10 to 12 (*right response curve*)

very low half-power frequency. The filter transfer function, Fig. 9, is entirely real (filtering preserves phase) and unity over a continuous frequency range including zero frequency (mean and trend); in the case of FFT only two discrete sinusoids would have appropriate frequency for the desired low pass.

After de-trending a Parzen (1961) window was applied to the sample autocovariance which in turn was separately computed over several non-overlapping segments (chunks) as indicated in Fig. 8, the periodograms were computed for all chunks and averaged. 2.5%/97.5% confidence limits always apply to the full length of the series. By contrast, for the simulation the solid line shows the PSD for the first six decades only which suggests that at least the simulated (and probably the observed) ENSO signal shows multi-decadal variations in amplitude.

At the high-frequency end both spectra are compatible with an inverse-square law as expected for a red noise background. At the present resolution both PSDs have a single broad peak which is at about 4 y for the observations and at about 28 months in the simulation. We stress that subdivision of each peak is a possibility, but only a much greater record length would permit the unambiguous discrimination of such a multimodal signal against a broadband process suggested by Fig. 8a, b. We performed a simple test by constructing a broadband AR(2) process (with homogeneous part $z_i - 1.68\ z_i - 1 + 0.75\ z_{i-2}$) driven by white Gaussian noise and found that in the estimated periodogram the true peak was split in two, even for relatively strong spectral smoothing. If the true spectrum actually is broadband, any spectrum estimator (e.g., maximum entropy method) is likely to misrepresent it (Kay and Marple 1981), in other words, a group of peaks may represent more broadband structure. On the other hand, failure to resolve two neighboring sharp peaks is also possible, thus neither the single peak null hypothesis nor alternatives can be rejected with confidence. Methodologically we note difficulties with the unambiguous identification of the often-cited bimodality in ENSO variance (Rasmusson et. al. 1990, Latif et al. 1992). In fact Barnett et al. (1995) have noted that the low-frequency mode has had a time scale attributed by various authors whose estimates spanned roughly a factor of two, and computed estimates from 26 to 40 months, which was part of their motivation subsequently to prefer the term 'principal spatial mode'. The present analysis of model and observations will provide results consistent with this concept.

4.2 Equatorial/off-equatorial zonal evolution

Before the statistical analysis we will examine the simulated tropical space-time variability in all three oceans in Fig. 10a, b showing Hovmoeller plots of unsmoothed monthly mean anomalies of SST and heat content of the upper 350 m averaged over the indicated latitude bands. The heat content was computed as the vertical integral of $\rho \times T$, which after the layer remapping reduces to a simple vertical summation. The first sixteen years of our analysis period are shown. In the Pacific, equatorial SST anomalies develop in the longitude range corresponding to the NINO3 region. Over the latter period this indicates significant phase-locking to the seasonal cycle. To resolve the imperfect simulation of SST anomalies in the east, we recall the preceding discussion of coastal upwelling. The low variability near the Peruvian coast would be consistent with insufficiently resolving coastal upwelling and hence variability

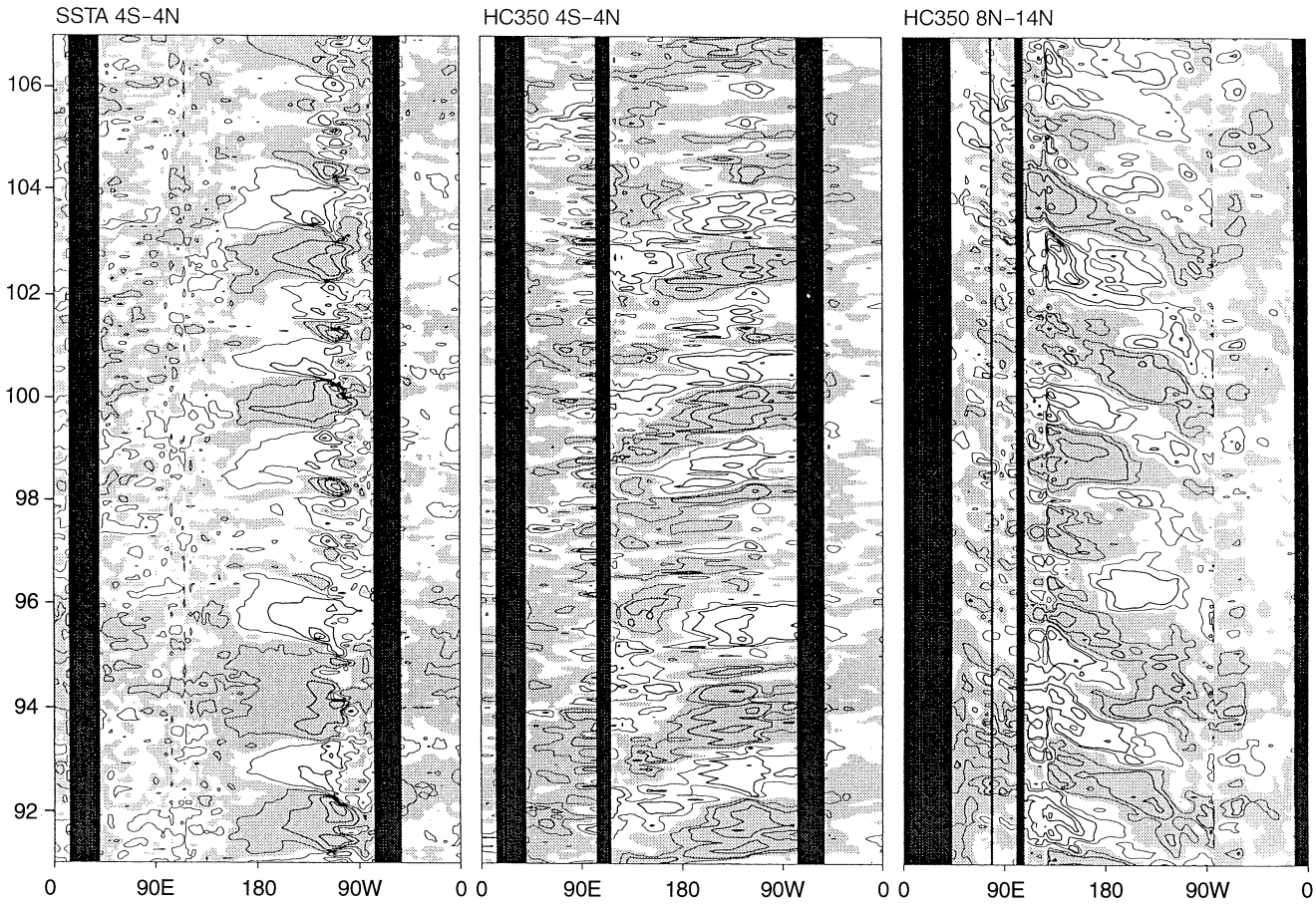

Fig. 10 Hovmoeller diagram of unsmoothed monthly mean anomalous SST (*left*) and heat content of the upper 350 m (*center* and *right*), averaged over latitude bands as indicated, for simulation y 91–106 as; contours at intervals of 1 K, 20 kg K cm^{-2}, resp. *Thin contours* indicate $\pm$ 0.3 K, 10 kg K cm^{-2}, respectively *Shading* indicates positive anomaly. *Ticks* mark the beginning of a year

thereof, with consequences for model stratus and the equatorial eastern Pacific as discussed in Sect. 3.2.

The region from where the model SST anomalies typically seem to spread, as expected from the preceding paragraph rarely extends significantly further east than about 100 °W. Typically, within at most a season it completes a westward spreading roughly up to the dateline, which in turn very occasionally is approached also from the west by anomalous SST, e.g., year 102. The latter, when it happens, exhibits relatively weak amplitude (about 0.3 K) compared to further east. By contrast, strong eastward propagating anomalies are typical for equatorial heat content. Although the rare cases of eastward SST propagation indicate correlation with heat content propagation, there are several counterexamples, such as year 98. Initially a propagation speed, corresponding to a basin crossing in six months could be ascribed to equatorial heat content signals. However, a typical characteristic speed as evident either from, e.g., year 98, or from the fine structure in longer lasting anomalies, implies basin crossing in closer to 3 or 4 months. Generally the arrival of equatorial heat content signals in the east correlates with the development of east Pacific SST anomalies. However near the western boundary, usually shortly before eastward propagation sets in, heat content signals have arrived off the equator at 8 to 14 °N that have travelled westward, often crossing the entire basin in about one year.

Altogether this picture is consistent with results from many coupled models with OGCM resolution sufficient to resolve equatorial waves, as far back as that of Schopf and Suarez (1988), and with spatio-temporal characteristics of observed ENSO as described in Latif et al. (1992). El Nino-type Eastern and Central Pacific SST variations dominate our model's tropical interannual variability and apparently are linked to equatorial wave dynamics with emphasis on the first few baroclinic modes, but with several equatorial wave excitations superimposed in most ENSOs, hence the fine-structuring of signals. Although this complexity precludes a detailed examination of the dispersion relation, the free modes available for producing the simulated dynamics in a linearized treatment are

eastward equatorial Kelvin and westward off-equatorial Rossby waves. The latter may be reflected at the western boundary into equatorial Kelvin signals with downwelling or upwelling character matching the incident wave. To form a self-sustained oscillation, a closed feedback loop involves equatorial upwelling and hence SST modified by arriving Kelvin waves, wind stress responding to SST changes and causing further build up of disturbances but simultaneously forcing oppositely signed off-equatorial Rossby waves. This scenario is presented in its simplest, point-coupling and single-mode, approximation by Suarez and Schopf (1988) and similarly by Battisti and Hirst (1989). Patterns emerging from our analysis, including zonal wind stress, are consistent with this general type of feedback. From the present analysis it is not possible to address fully the issue of eastward propagation in SST and other variables in both atmosphere and ocean which Barnett et al. (1991) focus on. The West Pacific portion of our diagrams suggests that a spatially more extensive analysis may be of considerable interest.

The Atlantic shows much weaker variability than the Pacific, but in equatorial heat content some lagged coherence with the Pacific is seen. For the Indian Ocean a dynamic link with the Pacific is not obvious in this spatially restricted representation.

4.3 Interrelation of dynamic forcing and thermal structure

We can now produce a less spatially selective description than is possible by Hovmoeller diagrams along latitudes (indeed reaffirming the choice of latitude), and include observed data. We concentrate on anomalous SST, zonal wind stress, and upper ocean heat content as the most important combination characterizing atmospheric forcing and ocean response on interannual scales (e.g., Neelin 1991; Latif et al. 1992; Schneider and Barnett 1995). Our aim is to decompose variability into spatial amplitude and phase patterns with amplitude and phase coefficient time series. For each variable we separately estimate complex empirical orthogonal functions (CEOFs; Barnett 1983; Horel 1984). This concept was originally derived from frequency domain principal component analysis (FDPCA, e.g., Brillinger 1981) where for a multivariate time series the spectrum matrix is diagonalized at various frequencies. Equivalently in the time domain, the time series, narrowly bandpass filtered, can be made complex-valued by adding, as an imaginary part, the result of advancing it by a temporal phase of 90 degrees. The complex-valued multivariate time series is then EOF-analyzed. With CEOFs the bandpass is widened or effectively omitted and 90 degrees lead is used in all Fourier components. In this broadband setup the method imposes no periodicity constraint as with each FDPC, however, if some frequency range is associated with maximum variance/spatial autocovariance, the leading pattern can capture the signal.

Figure 11a, b shows the leading CEOFs and associated principal components for the model and the GISST data. The filtering consists solely of the trend removal mentioned already and a lowpass of the type used to remove the GISST trend but with half-power at 1 year (see Fig. 9). The domain is restricted to a region equatorward of 22°, including the Indian ocean. The explained percentage of variance of the complex-valued time-dependent input field in filtered and (parenthesized) in unfiltered form is given. The second and third panels show the amplitude and phase of the complex principal component, below are maps for amplitude and phase of the leading pattern. An arbitrary constant phase can be added simultaneously to both the component and the spatial phase; for definiteness we imposed orthogonality of the real and the imaginary part of the pattern, with maximum variance in the real part. This constant phase determines the principal component real part shown in the top panel. With this choice of phase close agreement of the component with the NINO3 SST anomaly time series of Fig. 7 can be expected.

Zero spatial or component amplitude implies undefined phase and leads to disruptions in component phase, while the spatial phase may show singular points, as evident for the model. Thus the first point to notice is that locations of small amplitude and close-to-undefined phase agree well in model and observations, or conversely, similar regions contribute dominantly. The patterns in both cases explain about half of the (filtered) variance, and the variance reduction by filtering is similar. The mean amplitude over the Central and Eastern Pacific in both is also close (note separate but similar scales on the principal components), but the model has 1.2 units near the Peruvian coast where 2.4 are observed.

A number of higher resolution models miss the true spatial extent of the equatorial zone of maximum SST variance and underestimate it near the coast due mainly to overly strong equatorial upwelling and insufficient resolution near the coast (e.g., Robertson et al. 1995, Latif et al. 1994). In our model, resolution problems with respect to coastal upwelling have already been stated. We also recall that the simulation of vertical mixing and of the thermocline in the cold tongue is not perfect, and may show somewhat high sensitivity. During a warm heat content anomaly, the SST amplitude is locally exaggerated. As noted by Roeckner et al. (1996b) this has little impact on the atmospheric response due to the spatial confinement.

Included with the spatial phase are arrows parallel to the negative of the phase gradient at the arrow base indicating the direction of propagation for lines of constant phase whenever there is a negative rate of change of component phase. Evidently, for both model and observations apparent propagation is confined

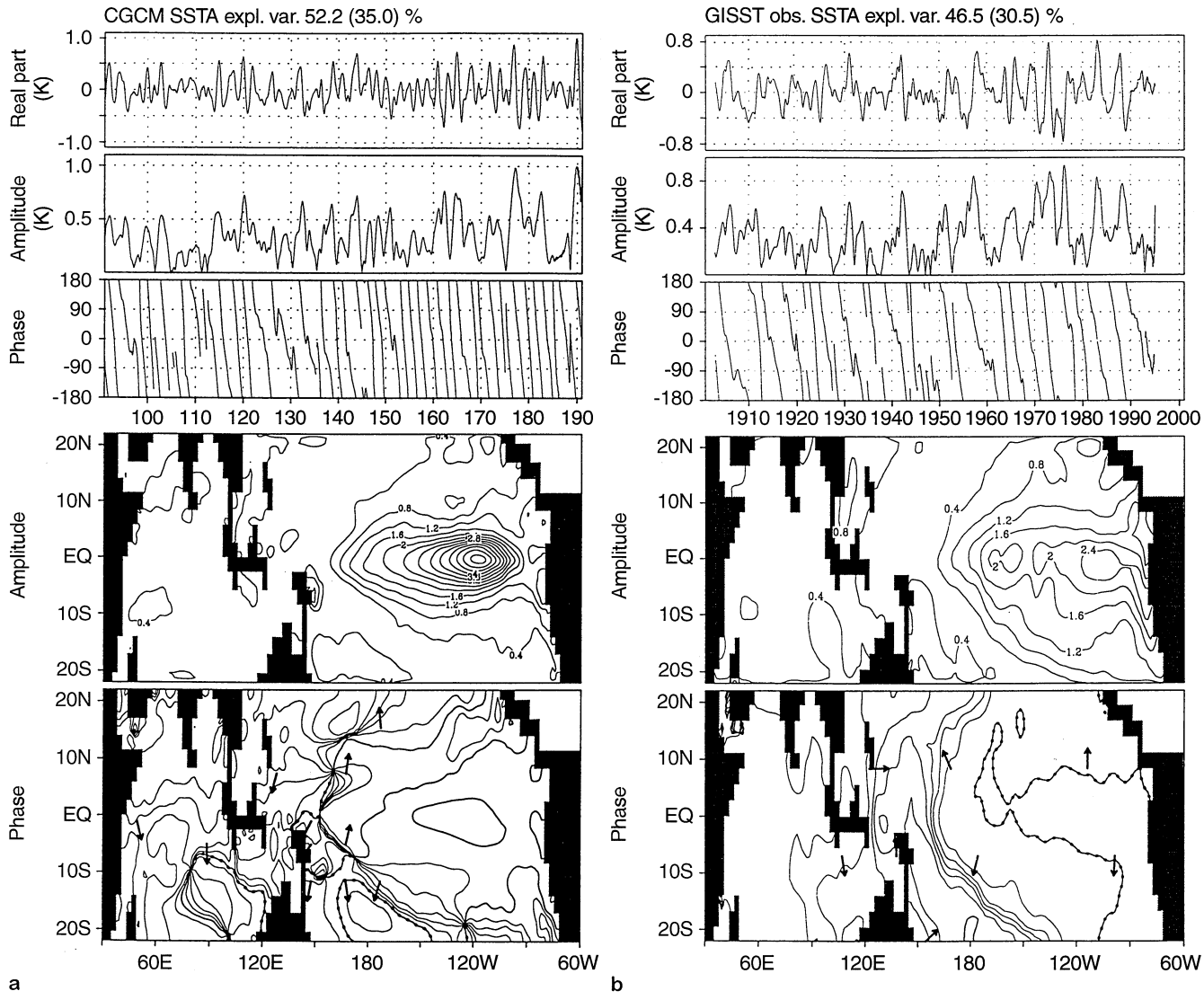

Fig. 11a, b Anomalous SST leading complex empirical orthogonal function (CEOF) (*bottom two panels*) and principal component time series real part, amplitude and phase (*top* 3 *panels*), **a** coupled model, **b** GISST 2.2 dataset. CEOF amplitude is dimensionless; CEOF phase contour interval is 30 °, with 0° and 180° *bold*, additionally the 0° contour is *dotted*. CEOF phase is shown with additional *arrows* anti-parallel to its gradient to indicate prevailing propagation direction (explanation see text). *Ticks* mark the beginning of a year

to regions with insignificant signal strength, maximum variance occurring at virtually constant phase. This suggests that for both model and observations a standing SST anomaly pattern results when a robust statistical description of ENSO variability is derived from as many realizations as possible. Note that single events or limited subsamples may well suggest a preferred mode involving propagation, but on the basis of the present extensive analysis, as opposed to the heat content (see later) the pattern found in the SSTA-CEOF will be referred to as essentially standing. An overall point shared by the two datasets, as already suggested by the explained variance fraction, is that none of the subsequent CEOFs was found to contain ENSO-related variability, the single exception being that the 1982/83 ENSO produces a peak in the second principal component, and correspondingly is slightly weaker in the first.

Regarding the upper ocean heat content (Fig. 12), the situation with observed data is considerably more difficult than for SST. The data represents temperature integrated over the upper 400 m as measured by expendable bathythermographs (XBT), gridded to $5^\circ \times 2^\circ$ (lon × lat) after spatial and temporal gaps have been filled (White 1995). We use the full record length but note the increase in samples during the 1970s and 1980s. Thus, when inspecting the component amplitude and phase with some caution, from about 1970

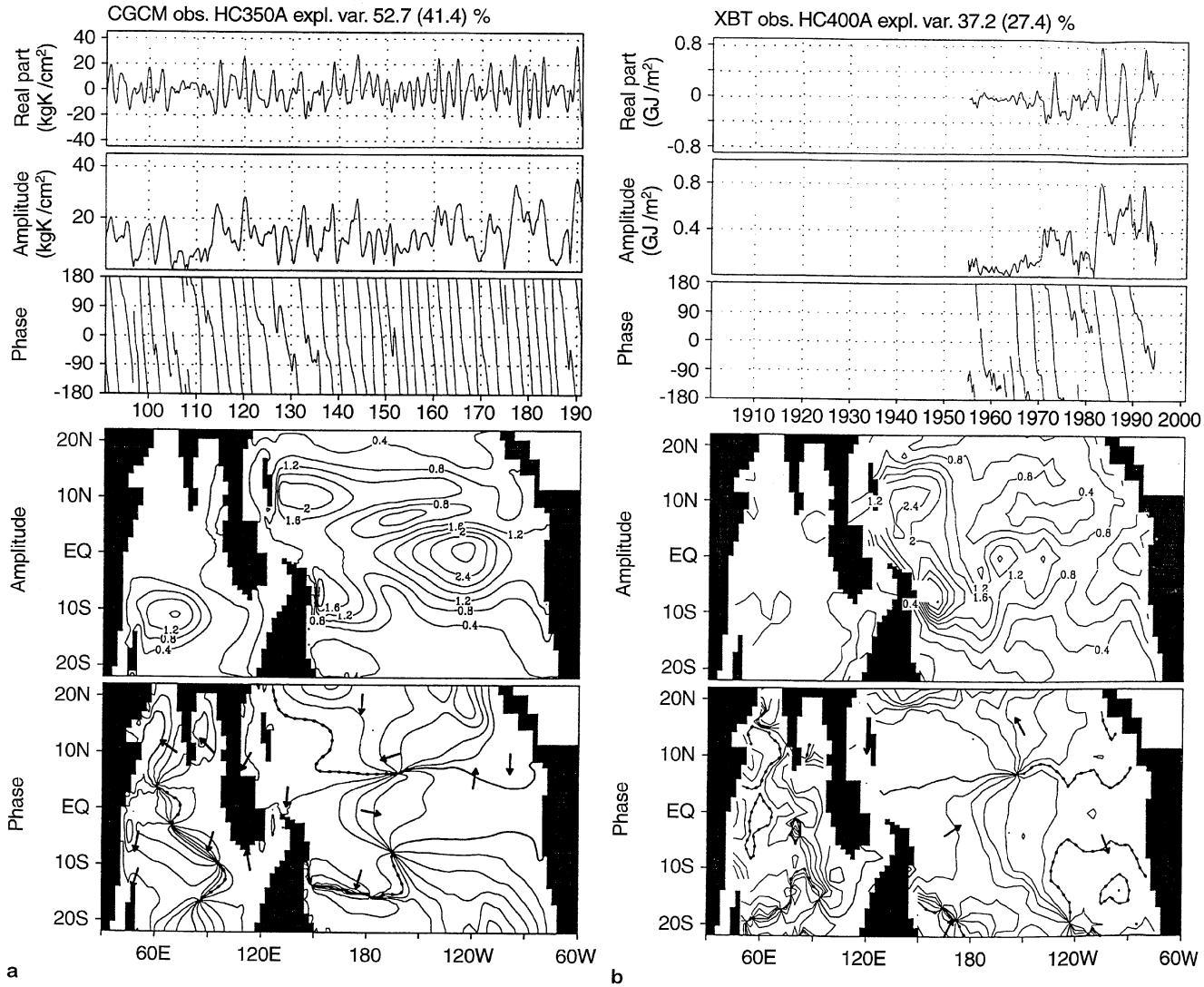

Fig. 12 As Fig. 10, but for upper ocean heat content. **a** Coupled model, upper 350 m (shallower areas omitted), **b** XBT data, upper 400 m

onwards we find quite good accordance with what was seen with the GISST data. The 1972, 1982 and 1986 ENSOs are also clearly present in the real part. Yet the agreement in component time series of SST and heat content is more clearly evident for the simulation results. For both datasets, however, the time series suggest that, apart from data uncertainties we again capture the ENSO signal remarkably well in the leading CEOF.

Turning to the spatial amplitude and phase, for both model and observations we find a rather similar structure in the Western and Central Pacific. The zone of maximum amplitude occupies a band of about 10 degrees latitudinal extent centered on the equator, and both datasets show a minimum of similar shape at about 8 °N and west of 110 °W. North of this minimum, about 10–12 °N (see Fig. 10, right hand panel), we see a prolonged zonal stretch of larger amplitude extending to the western boundary, where peaks of obvious similarity obtain, regarding shape and strength. A western boundary peak is also situated near 5°S. South of this latitude, weak amplitude is associated with phase noise. From this latitude northward, the phase has a pronounced basin-scale structure characterized by eastward propagation along the equator separated from a zone of westward propagation north of the aforementioned minimum. The lack of variance in part of the Eastern Pacific in the observations is most probably caused by sampling problems since the region in question is not frequently visited by ships. The apparently ENSO-related simulated peak in the Indian ocean is not clearly seen in the observations. It corresponds to a structure in zonal wind stress and is discussed later.

One could be tempted to combine the rate of change of the principal component phase and the phase gradient to form estimates of the phase speed e.g., on the equator, which would be larger in the simulation than in the observations. However, this will be subject to some distortion, since a single principal component phase is responsible for the entire domain, and examination e.g., of the phase lines approaching the western boundary shows that a zone of unphysical phase speed would result there. That such phase speeds do not always admit quantitative interpretation applies as well to other statistical methods for obtaining time-invariant complex-valued large-scale patterns. Moreover, in such methods a strict decomposition into single baroclinic modes is not achievable, but in the best case, as presented here, one obtains a representation of how, on average, energy propagates in a set of waves associated with an El Nino. The superposition of more than one signal in a simulated El Nino was indicated earlier by the fine structure in the apparent eastward propagation in Fig. 10.

The observed wind stress from the FSU atlas for the Pacific is used exclusively here since the Indian Ocean is only covered from 1970 through 1994. As with the XBT data, in Fig. 13 the component amplitude and phase, taking into account the weakened phase definition associated with zero or near zero amplitude, show reasonable agreement with those found in the case of the GISST data. It is noteworthy that the pattern contributes only a good quarter to the filtered variance. Its contribution to the raw variance is only 7.0% which implies that imposing half power at one year has reduced the total variance by almost a factor of four. This is not surprising with this atmospheric parameter, though, and feasible in the sense of essentially retaining the ENSO signal. Remarkably, very similar low pass fraction and explained variance percentage result in the simulation.

As expected, the pattern of both the observed and the simulated wind stress variability is dominated by a maximum on the equator centered virtually on the date line. The center regions agree well in strength, while the off-equatorial westward and eastward expanses are simulated stronger than observed. This positioning and strength is fully consistent with the composite analysis of zonal wind in Roeckner et al. (1996b). The equatorial zonal wind anomalies occur where during the second half of an ENSO year the ITCZ and the SPCZ merge and displace the southeast trades. This merging of convection zones is a further success of the model noted by Roeckner et al. (1996b).

In the Eastern Pacific, the maximum evident in the model at 120 °W is qualitatively similar to a weak observed structure. Similarly, observations and model both show the minimum west of this feature, as well as the maximum near 15 °S and the minimum near 15 °N. The simulated maximum in the Indian Ocean is nearly anticorrelated with the maximum at the date line; this phase relationship is consistent with the case of the heat content maximum in that basin whose location is west of the wind stress maximum. Since the Indian Ocean has been excluded from the CEOF of the FSU data, further investigation is in order to ascertain the correspondence with observed variability, as is an analysis of the Indian Ocean in isolation, to examine how much distortion possibly results from the inclusion of the strong Pacific ENSO variability.

To check to what extent a coherent signal in the present set of variables has been extracted for the simulation results, we examine the complex cross-correlation functions for the complex principal components (CPCs). These have maximum modulus, close to unity, at 0 months lag for SST and heat content, and at 1–2 months lead for windstress relative to heat content (Fig. 14). The latter is consistent with near-zero lag within the limits imposed by the previous low-pass filtering. To see the spatio-temporal coherence, recall that the arbitrary constant phase was determined by maximum variance in the real part of the pattern which implies assigning 0° and 180° to phase contours which exhibit least possible displacement from regions of large amplitude. Hence, choose locations of peak amplitude in the patterns of SST, wind stress, heat content at phase 180 °, 150–180 °, 0–30 °, respectively. These phases imply that the time evolution at these locations reconstructed from the leading CEOF resembles the principal component real part, with East Pacific warm SST in phase with westerly wind stress anomalies and cold (upwelling) off-equatorial as well as warm (downwelling) equatorial heat content anomalies (all have the component real part at negative extremes). Corresponding arguments apply to the observed CEOFs for the 1970s and 1980s (with reversed component real part signs and flipped spatial phase).

That the strength and spatial phasing of the ENSO-related variability in these key parameters emerges so clearly matched between our simulation and observations, suggests that our model captures a major proportion of relevant physics.

The mentioned preference for a time scale of about 28 months appears unrelated to local biennial mechanisms such as described by Meehl (1990,1992) and others, in view of the non-local feedback through wave dynamics which our work and other wave-resolving modelling studies have suggested as a key element. The phase speeds apparently characteristic in Fig. 10 best fit the second baroclinic mode, as expected for the adjustment of the upper ocean (e.g., Giese and Harrison 1990). Further factors to be analyzed are the strength and extent of equatorial as well as off-equatorial wind anomalies and the way they couple to SST gradients to initiate the build up of equatorial heat content anomalies. The present analysis can merely state that, in contrast to some models of at least equal resolution (e.g. the hybrid coupled models described in Barnett

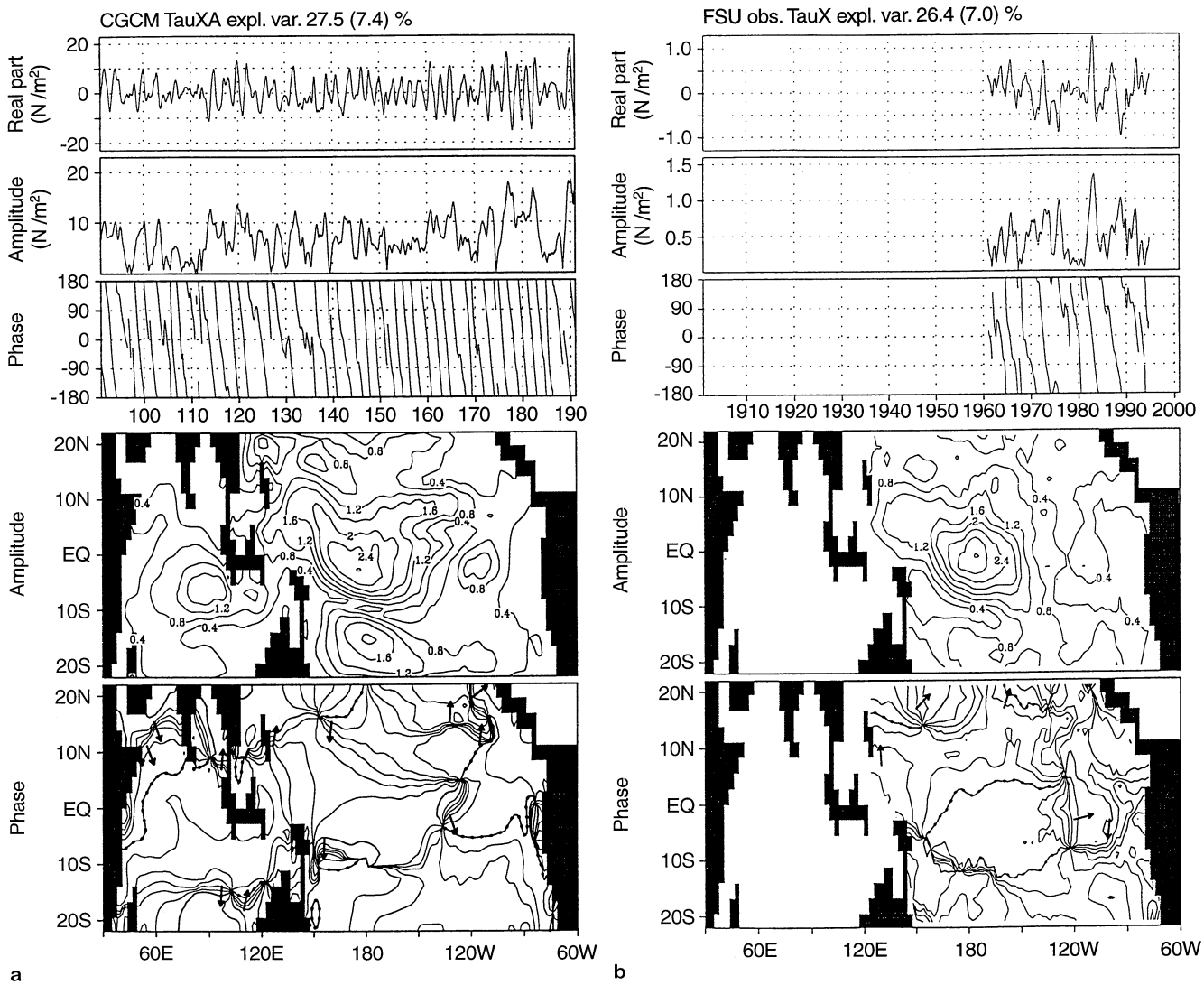

Fig. 13 As Fig. 10, but for zonal wind stress. **a** coupled model, **b** FSU data

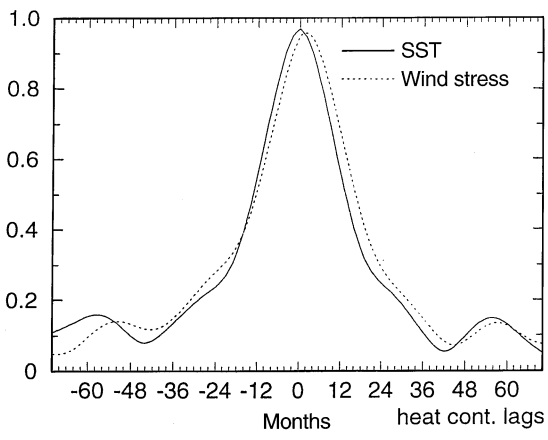

Fig. 14 Modulus of complex correlation of complex principal component time series in the coupled model for heat content-SST (*solid line*), and heat content-zonal wind stress (*dotted*)

et al. 1993, Syu et al. 1995), our model does not lock to the biennial frequency, despite overemphasizing it.

A characteristic time scale appears less well-defined in the GISST dataset in which, if anything, from about 1960 to 1990 the phase of the principal component appears to show a three-year time scale. This leading CEOF is rather stable when we vary the length of the record analyzed. To partially resolve the apparent inconsistency with the peak frequency in Fig. 8, an inspection of the component amplitude suffices, since even weak but non-zero amplitude has an associated phase progression but the spectral peak is largely positioned according to the strongest, somewhat less frequent, events. In actual fact, the principal component shows that even three years, or any sharply defined value, does not appear to be a universally applicable period through this dataset. We have presented our analyses having in mind that signal identification

should place significant emphasis on the spatial aspect as stressed also by Barnett et al. (1995).

5 Conclusions

In this work we validate the tropical Pacific seasonal cycle and interannual variability for the first 100 y of a multi-century simulation with a global atmosphere-sea ice-ocean general circulation model which employs non-seasonal heat and freshwater flux adjustment.

The simulation of the warm pool annual/semiannual cycle is encouraging and is accompanied by a mean state not predominantly forced by the flux adjustment. A major challenge for coupled GCMs, the mean cold tongue extent and the southeastern extent of the warm pool, is captured. In the east, the lack of realistic spring warming over several grid longitudes is linked to a too shallow thermocline which has to be investigated in more detail. On the other hand, we obtain a satisfactory vertical temperature distribution and overall current structure.

The AGCM stress is no weaker than observed and has an overall realistic pattern, and this is what makes it feasible to abandon flux adjustment for wind stress altogether. This is important for the links between simulated seasonal cycle and ENSO variability, since in particular seasonal wind stress adjustments can distort the phasing of equatorial wind stress anomalies, as discussed in Neelin et al. (1992). Also, Neelin and Dijkstra (1995) in an intermediate model obtain a bifurcation of a single stable state of tropical SST climatology into a bi-stable system with one rather realistic state and one with unrealistically high Eastern Pacific SST when flux adjustment of the wind stress is introduced with varying strength. Simulation of ENSO dynamics could thus become strongly distorted.

For sea surface temperature, zonal wind stress and upper ocean heat content, the model captures the dominant amplitude and phase patterns of the observed tropical Pacific ENSO signal as well as its strength. A strong candidate mechanism in the model is the non-local feedback by wind stress responding to anomalous SST gradient and modifying upwelling so as to reinforce the initial anomaly but simultaneously forcing off-equatorial anomalies of opposite sign. These exhibit wave-like propagation to the western boundary where shortly afterwards eastward propagating equatorial disturbances of like sign originate that counteract the initial anomaly. The prominent role these common characteristics play in both observations and simulation is our main reason for identifying the signal in the latter as ENSO. A validation of the global atmospheric response against the response of the AGCM to interannually varying observed SST was performed by Roeckner et al. (1996b). More frequent and not quite as irregular ENSO oscillations are simulated than observed. However, as to ENSO time scales, our analysis of anomalies in model and observations finds essentially a single amplitude/phase pattern and associated amplitude/phase time series, with time evolution most naturally described by a single maximum over a relatively broad frequency range rather than two or more narrowly defined frequencies, though the latter alternative cannot statistically be ruled out.

Acknowledgements This work has benefited a great deal from Prof. Lennart Bengtsson's continued interest and support. Two anonymous referees provided additional helpful comments. Part of this study was completed during a visit to the Scripps Institution of Oceanography, La Jolla, California, where support in both technical and scientific sense is gratefully acknowledged by A.B., as are the enjoyable and stimulating discussions with Timothy P. Barnett, Niklas Schneider and Arthur J. Miller. The XBT data were made available by W. B. White, Scripps Institution of Oceanography. The GISST dataset was provided by the British Meteorological Office. The initial coupled segment preceding the main model integration was tended by Ingo Kirchner of the Max-Planck-Institut für Meteorologie (MPI), Hamburg. Further stimulation came from discussion with Hans Graf and Mojib Latif, both at MPI. The model integration and much of the analysis were carried out on the Cray-C90 of the Deutsches Klimarechenzentrum (DKRZ), Hamburg. Financial support was given by the Bundesminister für Bildung und Forschung (BMBF) through the project 'Klimavariabilität und Signalanalyse', grant 07VKV01/1.

References

Barnett TP (1983) Interaction of the monsoon and Pacific trade wind systems at interannual time scales. Part I: the equatorial zone. Mon Weather Rev 111:756–773

Barnett TP, Latif M, Kirk E, Roeckner E (1991) On ENSO physics. J Clim 4:487–515

Barnett TP, Latif M, Graham NE, Flügel M (1992) Modal structure of variations in the tropical climate system. Part II: Origins of the low-frequency mode. MPI Rep 96, 30 pp, Max-Planck-Institut für Meteorologie, Hamburg, Germany

Barnett TP, Latif M, Graham N, Flügel M, Pazan S, White W (1993) ENSO and ENSO-related predictability. Part I: prediction of equatorial Pacific sea surface temperature with a hybrid coupled ocean-atmosphere model. J Clim 6:1545–1566

Barnett TP, Latif M, Graham N, Flügel M (1995) On the frequency-wave number structure of the tropical ocean/atmosphere system. Tellus 47A:998–1012

Battisti DS, Hirst AC (1989) Interannual variability in a tropical atmosphere-ocean model: influence of the basic state, ocean geometry and nonlinearity. J Atmos Sci 46(12):1687–1712

Brillinger DR (1981) Time series-data analysis and theory. Holden-Day, 540 pp

Brinkop S, Roeckner E (1995) Sensitivity of a general circulation model to parameterizations of cloud turbulence in the atmospheric boundary layer. Tellus 47A:197–220

Chen C-T, Roeckner E (1996a) Validation of the Earth radiation budget as simulated by the Max Planck Institute for Meteorology general circulation model ECHAM4 using satellite observations of the Earth Radiation Budget Experiment. J Geophys Res 101: 4269–4287

Chen C-T, Roeckner E (1996b) Warm pool heat budget as simulated by different versions of the ECHAM model. NATO ASI series, vol. I 34:95–105

Cubasch U, Hasselmann K, Höck H, Maier-Reimer E, Mikolajewicz U, Santer BD, Sausen R (1992) Time-dependent greenhouse warming computations with a coupled ocean-atmosphere model. Clim Dyn 8 : 55–69

Giese BS, DE Harrison (1990) Aspects of Kelvin wave response to episodic wind forcing, J Geophys Res 95, 7289–7312

Giorgetta M, Wild M (1995) The water vapour continuum and its representation in ECHAM-4. MPI Rep 162, 38 pp, Max-Planck-Institut für Meteorologie, Hamburg, Germany

Haney RL (1971) Surface thermal boundary condition for ocean circulation models. J Phys Oceanogr 1 : 241–248

Hibler WD III (1979) A dynamic thermodynamic sea ice model. J Phys Oceanogr 9 : 815–846

Horel JD (1982) On the annual cycle of the tropical Pacific atmosphere and ocean. Mon Weather Rev 110 : 1863–1878

Horel JD (1984) Complex principal component analysis: theory and examples. J Clim Appl Meteorol 23 : 1660–1673

Jin FF, Neelin JD, Ghil M (1994) El Nino on the devil's staircase: annual subharmonic steps to chaos. Science 264 : 70–72

Kay SM, Marple SL (1981) Spectrum analysis - a modern perspective. Proc IEEE 69(11) : 1380–1419

Knutson TR, Manabe S (1994) Impact of increased CO2 on simulated ENSO-like phenomena. Geophys Res Lett 21 : 2295–2298

Latif M, Barnett TP (1994) Causes of decadal climate variability over the North Pacific and North America. Science 266 : 634–637

Latif M, Barnett TP, Mizuno K (1992) Modal structure of variations in the tropical climate system. Part I: observations. MPI Rep 91, 26 pp, Max-Planck-Institut für Meteorologie, Hamburg, Germany

Latif M, Stockdale T, Wolff J, Burgers G, Maier-Reimer E, Junge M, Arpe K, Bengtsson L (1994a) Climatology and variability in the ECHO coupled GCM. Tellus 46A : 351–366

Lau NC, Philander SGH, Nath MJ (1992) Simulation of El Nino/Southern Oscillation phenomena with a low-resolution coupled general circulation model of the global ocean and atmosphere. J Clim 5 : 284–307

Levitus S (1982) Climatological atlas of the World Ocean. NOAA Prof Pap 13, US Government Printing Office, Washington, D.C., 173 pp

Lukas R, Lindstrom EJ (1991) The mixed layer of the western equatorial Pacific ocean. J Geophys Res 96 : 3343–3357

Lunkeit F, Sausen R, Oberhuber JM (1996) Climate simulations with the global coupled atmosphere-ocean Model ECHAM2/OPYC. Part I: present-day climate and ENSO events. Clim Dyn 12 : 195–212

Manabe S, Stouffer RJ, Spelman MJ, Bryan K (1991) Transient responses of a coupled ocean-atmosphere model to gradual changes of CO2. Part I: annual mean response. J Clim 4 : 785–818

Mechoso CR, Robertson AW, Barth N, Davey MK, Delecluse P, Gent PR, Ineson S, Kirtman B, Latif M, le Treut H, Nagai T, Neelin JD, Philander SGH, Polcher J, Schopf PS, Stockdale T, Suarez MJ, Terray L, Thual O., Tribbia JJ (1995) The seasonal cycle over the Tropical Pacific in coupled ocean-atmosphere general circulation models. Mon Weather Rev 123 : 2825–2838

Meehl GA (1990) Seasonal cycle forcing of El Niño-Southern Oscillation in a global coupled ocean-atmosphere GCM. J Clim 3 : 72–98

Meehl GA (1992) A coupled air-sea biennial mechanism in the tropical Indian and Pacific regions: role of the ocean. J Clim 6 : 31–41

Morcrette JJ (1991) Radiation and cloud radiative properties in the European Centre for Medium Range Weather Forecasts forecasting system. J Geophys Res 96 : 9121–9132

Murphy JM (1995) Transient response of the Hadley Centre coupled ocean-atmosphere model to increasing carbon dioxide. Part I: control climate and flux adjustment. J Climate 8 : 36–80

Nagai T, Tokioka T, Endoh M, Kitamura Y (1992) El Nino-Southern Oscillation simulated in an MRI atmosphere-ocean coupled general circulation model. J Clim 5 : 1202–1233

Neelin JD (1991) The slow sea surface temperature mode and the fast wave limit: analytic theory for tropical interannual oscillations and experiments in a hybrid coupled model. J Atmos Sci 48 : 584–606

Neelin JD, Dijkstra HA (1995) Ocean-atmosphere interaction and the tropical climatology. Part I: the dangers of flux correction. J Clim 8 : 1325–1342

Neelin JD, Latif M, Alaart MAF, Cane MA, Cubasch U, Gates WL, Gent PR, Ghil M, Gordon C, Lau NC, Mechoso CR, Meehl GA, Oberhuber JM, Philander SGH, Schopf PS, Sperber KR, Sterl A, Tokioka T, Tribbia J, Zebiak SE (1992) Tropical air-sea interaction in general circulation models. Clim Dyn 7 : 73–104

Neelin JD, Latif M, Jin FF (1994) Dynamics of coupled ocean atmosphere models: the tropical problem. Ann Rev Fluid Mech 26 : 617–659

Nordeng TE (1994) Extended versions of the convective parameterization scheme at ECMWF and their impact on the mean and transient activity of the model in the tropics. ECMWF Technical Memorandum No. 206, 41 pp., 1994

Oberhuber (1988) An atlas based on the "COADS" dataset: the budgets of heat, buoyancy and turbulent kinetic energy at the surface of the global ocean. MPI Rep 15, Max-Planck-Institut für Meteorologie, Hamburg, Germany

Oberhuber JM (1993) Simulation of the Atlantic circulation with a coupled sea-ice mixed layer-isopycnal general circulation model. Part I: model description. J Phys Oceanogr 13 : 808–829

Parzen E (1961) Mathematical considerations in the estimation of spectra. Technometrics 3 : 167–190

Philander SGH, Pacanowski RC, Lau NC, Nath MJ (1992) Simulation of ENSO with a global atmospheric GCM coupled to a high-resolution, tropical Pacific Ocean GCM. J Clim 5 : 308–329

Picaut J, Tournier R (1991) Monitoring the 1979–1985 equatorial Pacific current transports with expendable bathythermograph data. J Geophys Res 96 : 3263–3277

Rasmusson EM, Wang X, Ropelewski CF (1990) The biennial com ponent of ENSO variability. J Mar Sys 1 : 71–90

Rayner NA, Folland CK, Parker DE, Horton EB (1995) pers. comm. (A new global sea-ice and sea surface temperature (GISST) data set for 1903–1994 for forcing climate models. Hadley Centre Internal Note 69)

Reverdin G, Frankignoul C, Kestenare E, McPhaden MJ (1994) Seasonal variability in the surface currents of the equatorial Pacific. J Geophys Res 99, C10 : 20323–20344

Reinsch CH (1967) Smoothing by spline functions. Numerische Math 10 : 177–183

Robertson AW, Ma CC, Mechoso CR, Ghil M (1995a) Simulation of the tropical Pacific Climate with a coupled ocean-atmosphere general circulation model. Part I: the seasonal cycle. J Clim 8 : 1178–1198

Robertson AW, Ghil M, Mechoso CR (1995b) Simulation of the tropical Pacific Climate with a coupled ocean-atmosphere general circulation model. Part II: Interannual variability. J Clim 8 : 1199–1216

Roeckner E, Arpe K, Bengtsson L, Brinkop S, Dümenil L, Esch M, Kirk E, Lunkeit F, Ponater M, Rockel B, Sausen R, Schlese U, Schubert S, Windelband M (1992) Simulation of the present-day climate with the ECHAM model: Impact of model physics and resolution. MPI Rep 93, 171 pp, Max-Planck-Institut für Meteorologie, Hamburg, Germany

Roeckner E, Arpe K, Bengtsson L, Christoph M, Claussen M, Dümenil L, Esch M, Giorgetta M, Schlese U, Schulzweida U (1996a) The atmospheric general circulation model ECHAM-4: model description and simulation of present-day climate. MPI Rep 218, 90 pp, Max-Planck-Institut für Meteorologie, Hamburg, Germany

Roeckner E, Oberhuber JM, Bacher A, Christoph M, Kirchner I (1996b) ENSO variability and atmospheric response in a global coupled atmosphere-ocean GCM. Clim Dyn 12 : 737–754

Sausen R, Bartel K, Hasselmann K (1988) Coupled ocean-atmosphere models with flux correction. Clim Dyn 2 : 145–163

Sausen R, Schubert S, Dümenil L (1994) A model of river run-off for use in coupled atmosphere-ocean models. J Hydrol 155 : 337–352

Schneider N, Barnett TP (1995) The competition of freshwater and radiation in forcing the ocean during El Nino. J Clim 8 : 980–992

Schopf PS, Suarez MJ (1988): Vacillations in a coupled ocean-atmosphere model. J Atmos Sci 45 : 549–566

Suarez MJ, Schopf PS (1988) A delayed action oscillator for ENSO. J Atmos Sci 45 : 3283–3287

Stricherz JN, O'Brien JJ, Legler DM (1992) Atlas of Florida State University tropical Pacific winds for TOGA 1966–1985. The Florida State University, Mesoscale Air-Sea Interaction Group, Tallahassee, Florida

Stricherz JN, O'Brien JJ, Legler DM (1993) Atlas of Florida State University Indian Ocean winds for TOGA 1970–1985. The Florida State University, Mesoscale Air-Sea Interaction Group, Tallahassee, Florida

Syu H, JD Neelin, D Gutzler (1995) seasonal and interannual variability in a hybrid coupled GCM. J Clim 8 : 2121–2143

Tett S (1995) Simulation of El Nino-Southern Oscillation-like variability in a global AOGCM and its response to CO_2 increase. J Clim 8 : 1473–1502

White WB (1995) Design of a global observing system for gyre-scale upper ocean temperature variability. Progr Oceanogr 36(3) : 169–217

Wyrtki K, Kilonsky B (1984) Mean water and current structure during the Hawai-to-Tahiti shuttle experiment, J Phys Oceanogr 14 : 242–254